Fabrication of a 2.8 v high-performance aqueous flexible fiber-shaped asymmetric micro-supercapacitor based on MnO2/PEDOT:PSS-reduced graphene oxide nanocomposite grown on carbon fiber electrode

# Fabrication of a 2.8 V high-performance aqueous flexible fiber-shaped asymmetric micro- supercapacitor based on $MnO_2$/PEDOT:PSS-reduced graphene oxide nanocomposite grown oncarbon fiber electrode†

Leila Naderi,[ab] Saeed Shahrokhian *[bc] and Francesca Soavi *[a]

[a]*Department of Chemistry "Giacomo Ciamician", Alma Mater Studiorum-Universita` di Bologna, Via Selmi 2, 40126, Bologna, Italy. E-mail: francesca.soavi@unibo.it*

[b]*Department of Chemistry, Sharif University of Technology, Tehran 11155-9516, Iran. E-mail: Shahrokhian@sharif.edu*

[c]*Institute for Nanoscience and Technology, Sharif University of Technology, Tehran, Iran*

Flexible and lightweight fiber-shaped micro-supercapacitors have attracted tremendous attention as next- generation portable electronic devices, due to their high flexibility, tiny volume, and wearability. Herein, we successfully fabricated a ternary binder-free nanocomposite of $MnO_2$/PEDOT:PSS–rGO on a carbon fiber substrate for application in high performance fiber-shaped micro-supercapacitors. The synergistic effects of the different components in the fiber-shaped electrode help to deliver a high specific capacitance of 2.9 F $cm^{-2}$ (194 F $cm^{-3}$ and 550 mF $cm^{-1}$) at a current density of 5 mA $cm^{-2}$ and a long cycle life with 95%capacitance retention after 5000 cycles in 1 M $Na_2SO_4$ electrolyte. A fiber-shaped asymmetric micro- device based on the resulting hybrid electrode was assembled. A maximum energy density of $E_A$ ¼ 295microW h $cm^{-2}$ ($E_V$ =19 mW h $cm^{-3}$) and power density of $P_A$ = 14 mW $cm^{-2}$ ($P_V$ = 930 mW $cm^{-3}$) wereachieved in an operating voltage window of 0–2.0 V in a solid-state $Na_2SO_4$–CMC electrolyte.
Moreover, a fiber-shaped asymmetric micro-device with a super-concentrated potassium acetate-based water-in-salt electrolyte (27 m KOAC) is presented. The use of the water-in-salt electrolyte enables a cellvoltage of 2.8 V, and energy densities are higher than those of the micro-device operating with conventional dilute aqueous electrolytes.

## 1. Introduction

With rapidly growing demand for next-generation portableelectronics such as roll-up displays, photovoltaic cells andwearable devices, more and more attention has been devoted tothe development of flexible and lightweight energy storage equipment.[1–9] Fiber-shaped micro-supercapacitors are the most promising flexible energy storage devices for next-generationportable and wearable electronics, due to their higher power density, light weight, tiny volume, extraordinary flexibility and remarkable wearability.[10–12] However, they suffer from low energy densities, which have greatly restricted their applica- tions in next-generation energy storage devices.[13–16] Accordingto the formula $E$ ¼ $1/2CV^2$, improving the specific capacitance and expanding the operating voltage range are highly efficient routes to enhance the energy density of supercapacitors. The specific capacitance of micro-supercapacitors mainly relies onthe inherent features of electrode materials, including high surface area, superior electrical conductivity, unique nano-structure architecture and high chemical stability. The fabrication of asymmetric micro-supercapacitors can be consideredan extremely expedient method to widen operating voltage by using different working potential windows of two electrodes inthe same electrolyte system and thus increasing their energy density.[17,18]
Electrolytes also play a critical role in determining the operating voltage and the overall performance of micro- supercapacitors. The ionic liquids and organic electrolytes usually have wider potential stability windows (>3.0 V), whichnotably enhances the energy density. However, the lower conductivity and higher

viscosity of ionic liquids (ILs) and the cost.[19–22] Consequently, aqueous electrolytes are receiving complex assembly process, which increases the fabrication toxicity and flammability of organic electrolytes have limited their applications in micro-supercapacitors. Also, considering the sensitivity of ILs and organic electrolytes to moisture,supercapacitors require ultradry storage condition and a complex assembly process, which increases the fabrication cost.[19–22] Consequently, aqueous electrolytes are receiving intensive attention due to their high conductivity, low cost, intrinsic non-flammable nature, and environment friendliness.

Nonetheless, their use is limited due to the narrow electro- chemical stability window of water (pure water decomposes above 1.23 V).[23,24] Recently, super-concentrated water-in-salt (WIS) electrolytes were proposed as a new strategy to widen the potential window of aqueous solutions to ~3 V. The super-concentrated aqueous solution suppresses the electrochemical activity of the water molecules through decreasing the content of free water in the WIS electrolyte. This effectively hinders the decomposition of water molecules near the cathode or anode, thereby widening electrochemical stability window.[25–27] The first reported WIS electrolyte was prepared using 20 m (mol $kg^{-1}$) aqueous solution of lithium bis(trifluoromethane sulfonyl) imide (LiTFSI), which exhibited a wide electrochemical stability window of ~3.0 V on stainless steel electrodes.[28] However, high cost and high toxicity of WIS electrolytes based on imide salts limit their practical applications. Recently, it was found that WIS electrolytes based on potassium acetate (KOAC) show higher ionic conductivities (>20 mS $cm^{-1}$) than LiTFSI electro-lytes (<10 mS $cm^{-1}$), which is due to the weak Lewis acidity of potassium ions or weak interaction of acetate anions.[29,30] Gogotsi *et al.* reported a 21 m KOAC-based WIS electrolyte for high-voltage aqueous asymmetric supercapacitors.[31] However,the voltage of the assembled supercapacitor using this electrolyte was 2.2 V. Also, most current collectors used in WIS electrolytes are not suitable for the design of flexible and micro-sized energy storage devices.

Similar to conventional supercapacitors, fiber shaped micro-supercapacitors, can be divided into three types according to their charge storage mechanisms: electric double layer capacitors (EDLCs), pseudocapacitors, and hybrid supercapacitors.[32,33] EDLCs store energy by electrostatic accumulation of charges atthe electrode/electrolyte interface. This non-Faradaic process This non-Faradaic process gives rise to what is called double-layer capacitance. Unlike EDLCs, pseudocapacitors store electrochemical energy via reversible and fast electrode redox reactions. When these processes give rise to an electrochemical response similar to that of EDLCs (i.e. linear relation between stored charge and voltage), electrode materials are termed pseudocapacitive. Also, hybrid supercapacitors store energy by combining both EDLC and pseudocapacitance processes. Carbon-based materials such as graphene and carbon nanotubes are widely used as electrode materials for EDLCs and possess a long cycle life. Metal oxides and conducting polymers (e.g., PEDOT:PSS) are typical pseudocapacitance materials, and have a high theoretical capacitance.34–37 PEDOT:PSS is considered a promising material for micro-supercapacitors, mainly owing to its good chemical and electrochemical stability, high conductivity, lowmaterial cost and excellent dispersibility in various solvents. However, the low specific capacitance of PEDOT:PSS hinders its wide application, which can be due to the relatively low ionic conductivity of the active materials.38–

43 To solve this problem, an effective strategy is combining it with conductive materials, such as reduced graphene oxide (rGO), which possesses a high capacitance and extremely long cycle life, because of its chemical stability, good

EDLC and ultrahigh specific surface area.44–46 Moreover,MnO2, as an active material for the positive electrode is an attractive candidate for micro-supercapacitors due to its low cost, wide electrochemical potential window, and high theoretical specific capacitance (1370 F $g^{-1}$).[45–50] Zhou *et al.* prepared $MnO_2$ nano-sheets on zeolitic imidazolate framework-67 derived N-doped carbon conductive skeletons. The prepared electrode exhibited a remarkable capacitance of 1483.5 mF $cm^{-2}$ at 2 mA $cm^{-2}$.[51] In another study, Zhou *et al.* reported Na-doped $MnO_2$ nanosheets on carbon nanotube fiber as a cathode electrode material for supercapacitor applications. The Na–$MnO_2$ NSs/CNTF showed a specific capacitance of 845 mF $cm^{-2}$ at 2 mA $cm^{-2}$.[52] The constructed ternary composite electrodes could combine the merits of each component and enhance the electrochemical performance of the energy storage systems. For example, Sun *et al.* prepared a PPy/PEDOT:PSS@MWCNT/SF composite elec-trode by drop coating of PEDOT:PSS and MWCNTs onto silk fabrics and then electro-polymerization of PPy, which exhibits a specific capacitance of 5296 mF $cm^{-2}$ at 2 mA $cm^{-2}$ in aqueous

electrolyte.[42] Yan *et al.* synthesized a $MnO_2$/rGO/PEDOT:PSS electrode by dispersing the $MnO_2$/rGO precursor in the PEDOT:PSS solution. Then, the composite was mixed with carbon black and polytetrafluoroethylene (PTFE) and pressed onto a nickel foam substrate. The electrochemical performance of this electrode has been evaluated only in a three-electrode system, and it exhibited a specific capacitance of 169.1 F $g^{-1}$ at 0.2 A $g^{-1}$ in 1 M $Na_2SO_4$ electrolyte.[46] Indeed, the use of a polymeric binder and conductive additive increases the internal resistance of the electrode and hinders its potential application in high perfor- mance supercapacitors. Moreover, compared to other conductive substrates such as Ni foam, carbon cloth, and metal foils, carbon fiber with characteristics such as excellent flexibility, light weight, good mechanical strength and exceptional conductivity, is an ideal fiber-shaped substrate for the growth of electroactive materials. To our knowledge, this is the first report that describes a fiber-shaped asymmetric micro-device based on a $MnO_2$/ PEDOT:PSS–rGO composite grown on a flexible carbon fiber substrate in conventional dilute aqueous and 27 m KOAC-based WIS electrolytes.

Herein, we used carbon fiber (CF) as a flexible micro-sized substrate for growth of the electrode materials. The $MnO_2$/ PEDOT:PSS–rGO composite electrode was prepared by the electrodeposition of $MnO_2$ on conductive CF composites, fol- lowed by drop-coating a mixture of PEDOT:PSS and rGO. The results of the materials morphology and structure obtained by FE-SEM, XRD and FTIR analyses are reported and discussed. The full electrochemical characterization of the eletrodes in 1 M $Na_2SO_4$ electrolyte is presented, and the performance of the solid-state micro-device assembled with $MnO_2$/PEDOT:PSS–rGO and PEDOT:PSS–rGO as positive and negative electrodes and $Na_2SO_4$–CMC electrolyte is reported for the first time. In addition, a micro-device assembled with the $MnO_2$/PEDOT:PSS–rGO fiber electrode and 27 m KOAC-based WIS electrolyte, operating at 2.8 V, is proposed here for the first time to our knowledge.

## 2. Experimental section

### 2.1. Chemicals

Potassium acetate ($CH_3CO_2K$, >99%), manganese acetate tet rehydrate ($Mn(CH_3COO)_2\ 4H_2O$, >99%) carboxymethyl cellulose sodium (average $M_w \sim 90\ 000$), and sodium sulfate decahydrate ($Na_2SO_4 10H_2O$, > 99%) were purchased from Sigma-Aldrich Company. Reduced graphene oxide was from Nanoinnova Technologies. Preparation of $MnO_2$/PEDOT:PSS–rGO@CF. Firstly, carbon fiber (diameter of 0.6 mm) was cleaned by sonication for 15 min consecutively in 2 M HCl solution, absolute ethanol, acetone and deionized MilliQ water, to remove surface oxides and contaminants, and then dried at room temperature. PEDOT:PSS was dispersed in deionized (DI) water and alcohol solution and sonicated for 15 min at room temperature. Next, 2 mL PEDOT:PSS dispersion solution was added to 2 mg rGO. The mixed solution PEDOT:PSS–rGO was drop-coated on carbon fiber and allowed to stay at the indoor temperature for 10 min. Then, the prepared electrode was dried at 60 °C for 1 h. $MnO_2$ was then electrodeposited on the PEDOT:PSS–rGO@CF electrode in the electrolyte solution containing 0.1 M manganese acetate at a current density of 10 mA $cm^{-2}$ for time 40 min. The prepared electrode was rinsed several times with deionized MilliQ water and then dried in an oven at 60 °C for 1 h. For comparison, the $MnO_2$@CF electrode was prepared using direct deposition of $MnO_2$ on the carbon fiber current collector. The mass loading of $MnO_2$/PEDOT:PSS–rGO, PEDOT:PSS–rGO, $MnO_2$/PEDOT:PSS and $MnO_2$ active materials loaded on the carbon fiber substrate was 0.6, 0.55, 0.5, and 0.5 mg $cm^{-1}$, respectively.

### 2.3. Fabrication of the all-solid-state asymmetric microdevice

The all-solid-state asymmetric micro-device was fabricated using MnO2/PEDOT:PSS–rGO@CF and PEDOT:PSS–rGO@CF as positive and negative electrodes, respectively, and Na2SO4–carboxymethyl cellulose sodium (CMC) gel as the solid state electrolyte.

The Na2SO4–CMC gel electrolyte was prepared by dissolving 3.55 g of Na2SO4 and 1.5 g of CMC in 50 mL of deionized water and heated at 85 C for 1 h under vigorous stirring until the gel solution became clear. The positive and negative electrodes and separator were soaked in the Na2SO4–CMC gel electrolyte for 15 min, and then the constructed microdevice was dried at room temperature for several hours to evaporate excess water from the solid-state electrolyte.

### 2.4. Preparation of the water-in-salt electrolyte

The potassium acetate (KOAC) electrolyte with a concentration of 27 m was prepared by dissolving appropriate amounts of KOAC salt in deionized MilliQ water at room temperature under stirring. The unit of the water-in-salt electrolyte was “m” as an abbreviation of mol kg 1 for molality.

### 2.5. Materials characterization

The surface morphology of the MnO2/PEDOT:PSS–rGO@CF, PEDOT:PSS–rGO@CF, MnO2@CF and PEDOT:PSS@CF electrodes was characterized by using a field-emission scanning electron microscope (FE-SEM MIRA 3 TESCAN, 15 kV, Czech) equipped with an energy dispersive X-ray (EDX) analyzer. The crystal structure of the prepared samples was investigated by Xray diffraction (XRD), using Cu Ka radiation and a Philips X'PERT diffractometer. Fourier transform infrared spectra (FTIR) of the samples were recorded on a PerkinElmer FT-IR spectrophotometer (spectrum 100). The surface area and pore size distribution of the samples were estimated by Brunauer–Emmett–Teller (BET) and Barrett–Joyner–Halenda (BJH) procedures using a Quantachrome Instrument (NOVA station).

2.6. Electrochemical characterization

Cyclic voltammetry (CV), galvanostatic charge–discharge (GCD) and electrochemical impedance spectroscopy (EIS) measurements were conducted by using a VSP multichannel potentiostat/galvanostat/FRA (BioLogic). EIS measurements were performed at a frequency ranging from 0.1 Hz to 100 kHz with a potential amplitude of 5 mV. The electrochemical properties of the individual electrodes were measured in a threeelectrode system, with 1 M Na2SO4 as the electrolyte, Pt wire as the counter electrode and Ag/AgCl as the reference electrode.

The supercapacitor performance was evaluated by using a 2-electrode setup. The length, areal, and volumetric specific capacitances (C) were calculated from the GCD curves and the formula as follows:53

$$C_{\mathrm{L}} = \frac{i\Delta t}{L\Delta V} \tag{1}$$

$$C_{\mathrm{A}} = \frac{i\Delta t}{(\pi DL)\Delta V} \tag{2}$$

$$C_{\mathrm{V}} = \frac{i\Delta t}{(0.25\ \pi D^2 L)\Delta V} \tag{3}$$

where CL (F cm  1) is the length specific capacitance, CA (F cm-2) is the areal specific capacitance, CV (F cm  3) is the volumetric specific capacitance, Dt (s) is the discharge time, i (A) is the discharge current, DV (V) is the potential window, and L and D are the geometric length and diameter of the carbon fiber electrode.

Also, the specific capacitance of electrodes and the supercapacitor was calculated from CV curves by using the following equation:

$$C = \frac{\int i\mathrm{d}V}{(Xv\Delta V)} \tag{4}$$

Here y is the scan rate (V s 1), i is current (A), X . L, A, and V are the length, areal, and volume of the electrode, respectively. The energy density and power density delivered by the microsupercapacitor were calculated by using eqn (5) and (6).

$$E_X = \frac{C_X V^2}{7200} \quad (5)$$

$$P_X = \frac{E_X \times 3600}{\Delta t} \quad (6)$$

Here $E_x$ ¼ $E_L$, $E_A$, $E_V$, which are the length ($E_L$, W h cm$^{-1}$), areal ($E_A$, W h cm$^{-2}$), and volumetric ($E_V$, W h cm$^{-3}$) energy density, $P_x$ ¼ $P_L$, $P_A$, and $P_V$ are the length ($P_L$, W cm$^{-1}$), areal ($P_A$, W cm$^{-2}$), and volumetric ($P_V$,W cm$^{-3}$) power density, respectively, and D$t$ is the discharge time in units of seconds.

## 3. Results and discussion

### 3.1. Characterization of the $MnO_2$/PEDOT:PSS–rGO@CF

A schematic illustration for the synthesis of the $MnO_2$/ PEDOT:PSS–rGO nanocomposite on the carbon fiber substrate is presented in Fig. 1. At first, a mixture of rGO and PEDOT:PSS was cast on the carbon fiber substrate. Then, the $MnO_2$ nano-flakes were electrochemically deposited on the PEDOT:PSS–rGO electrode by applying a constant current density of 10 mA cm$^{-2}$.

The morphologies of $MnO_2$, PEDOT:PSS, PEDOT:PSS–rGO, and $MnO_2$/PEDOT:PSS–rGO samples grown on carbon fibers were investigated by FE-SEM and the collected images are shown in Fig. 2. Fig. 2A and B show that the carbon fiber after the cleaning process features a smooth surface. Fig. 2C and D show that PEDOT:PSS/CF carbon fibers are tightly covered with a thin layer of polymer. Fig. 2E–H depict the FE-SEM images of PEDOT:PSS–rGO at different magnifications. The wrinkled features of the graphene nanosheets can be clearly observed, which provide a high surface area on the electrode surface. The FE-SEM images of $MnO_2$ and $MnO_2$/PEDOT:PSS–rGO samples show that $MnO_2$ nanomaterials are highly porous and made of many tiny nano flakes that are axially grown on the structure of carbon fiber (Fig. 2I–L). The creation of such a structure can be favorable for fast electron transfer and electrolyte ion diffusion during the charge–discharge process.

The elemental composition of the prepared electrode was investigated by EDX analysis (Fig. 3A). The EDX analysis demonstrates weight percentages of 66.02% C, 24.99% O, 0.05% S and 8.93% Mn elements in the $MnO_2$/PEDOT:PSS– rGO@CF electrode. The $N_2$ adsorption–desorption isotherm of the $MnO_2$/PEDOT:PSS–rGO composite suggests a typical IV-type curve (Fig. 3B), presenting a high surface area of 83 m$^2$ g$^{-1}$ and total pore volume of 0.2 cm$^3$ g$^{-1}$. Notably, the presence of both micro- and meso-pores in the structure of the $MnO_2$/ PEDOT:PSS–rGO composite is further confirmed by the pore size distribution curve (inset in Fig. 3B).

The phase structure of the rGO–PEDOT:PSS and $MnO_2$/ PEDOT:PSS–rGO composites was studied by the XRD analysis and the results are reported in Fig. 4A. In order to perform the XRD analysis, the $MnO_2$/PEDOT:PSS–rGO composite was scratched from the carbon fiber substrate. The diffraction peaks for the PEDOT:PSS–rGO sample observed at 25° and 47° are related to rGO. The XRD pattern of the $MnO_2$/PEDOT:PSS–rGOcomposite shows diffraction peaks at 37.4°, 42.8° and 56.4°which can be indexed to (101), (111) and (211) planes oftetragonal phase $MnO_2$ in $P4_2/mnm$ with standard lattice constants: $a$ ¼ 4.44 Å, $b$ ¼ 4.44 Å and $c$ ¼ 2.89 Å (b ¼ 90°) (JCPD no. 004-0779).

The FT-IR spectra of PEDOT:PSS–rGO and $MnO_2$/PEDOT:PSS–rGO nanocomposites are presented in Fig. 4B. For the PEDOT:PSS–rGO composite, the observed bands at 1620 and 1380 $cm^{-1}$ are attributed to vibrations of C═══C and C–C bonds of the thiophene ring and C═══O in the carboxylic acid and carbonyl groups. Also, the band at 1120 $cm^{-1}$ is attributed to the $–SO_3H$group of PSS. The broad band observed in the region of 3412 $cm^{-1}$ can be ascribed to the stretching vibration of O–H groups. The presence of the peaks in the composite spectra indicates p–p interaction between rGO and PEDOT:PSS. In thecase of $MnO_2$/PEDOT:PSS–rGO, in addition to the presence of characteristic peaks of rGO and PEDOT:PSS, the observed band at552 $cm^{-1}$ is attributed to the Mn–O vibration mode.

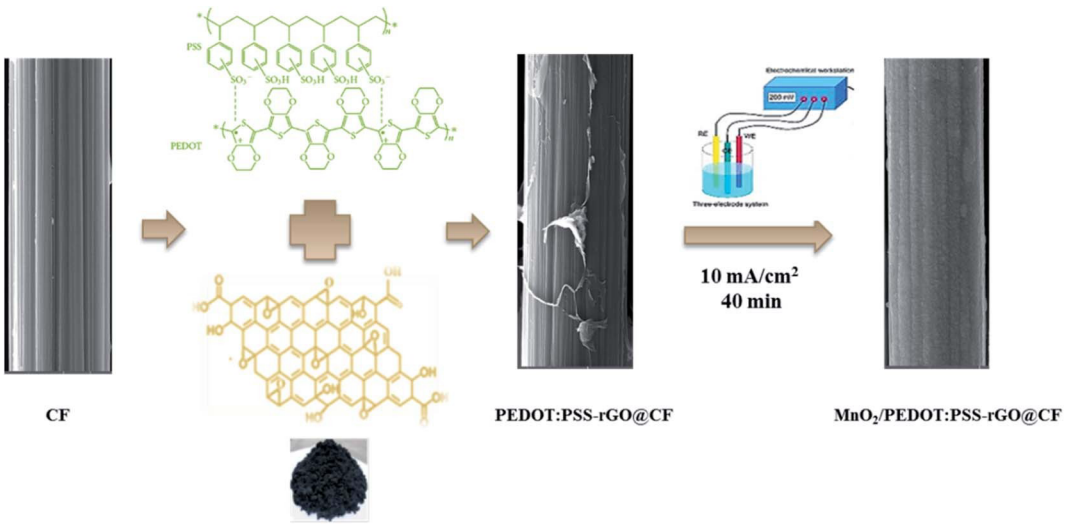


Fig. 1 Schematic representation of $MnO_2$/PEDOT:PSS–rGO@CF electrode preparation.

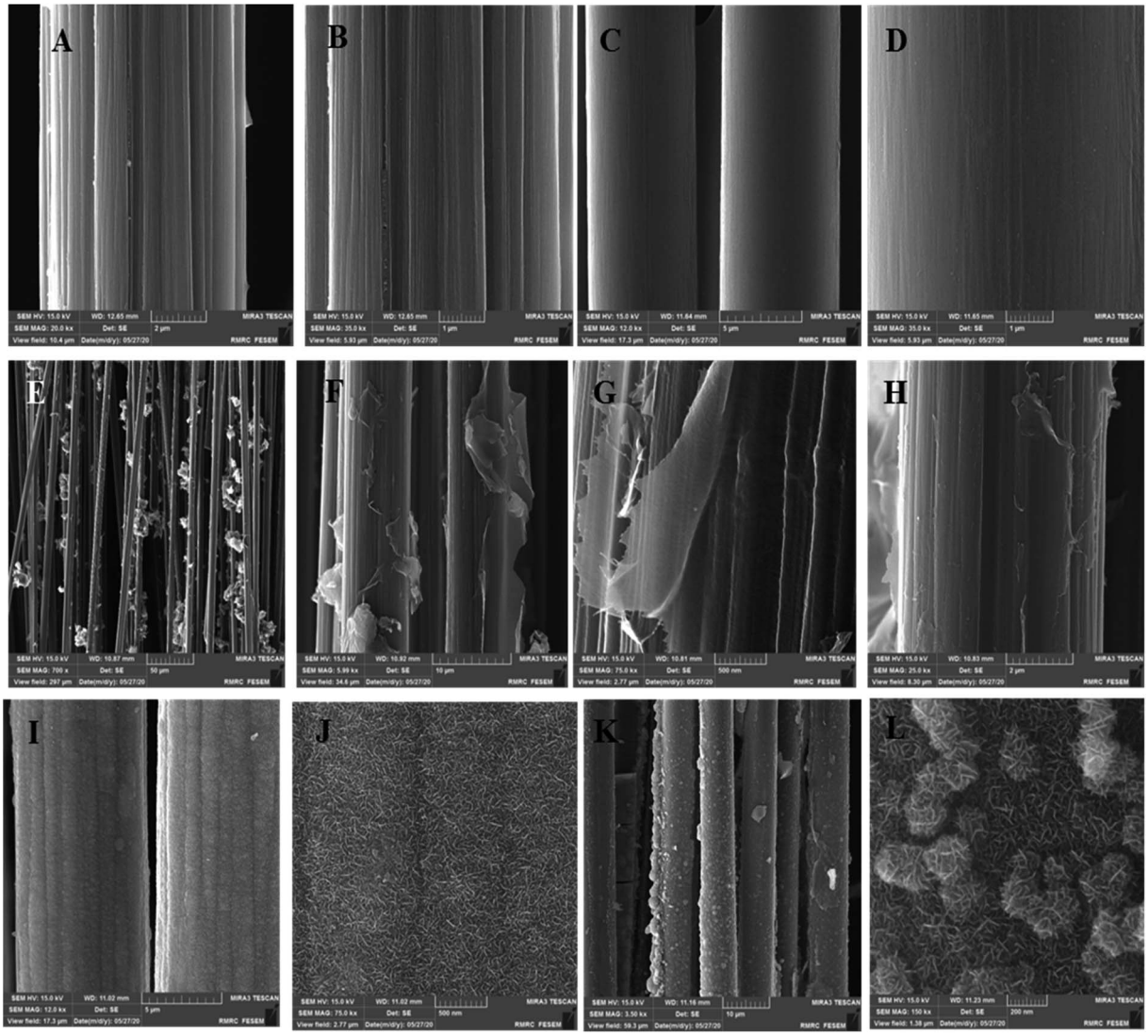


Fig. 2 FE-SEM images of (A and B) CF, (C and D) PEDOT:PSS/CF, (E–H) PEDOT:PSS–rGO/CF, (I and J) $MnO_2$/CF, and (K and L) $MnO_2$/PEDOT:PSS–rGO/CF at different magnifications.

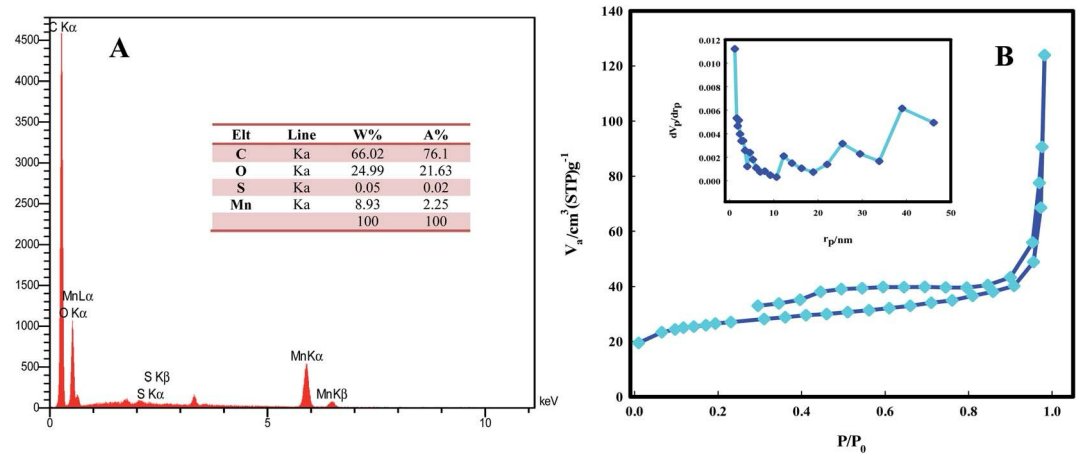


Fig. 3 (A) EDX spectra and (B) $N_2$ adsorption–desorption isotherm of the $MnO_2$/PEDOT:PSS–rGO nanocomposite (inset: the corresponding BJHpore size distribution).

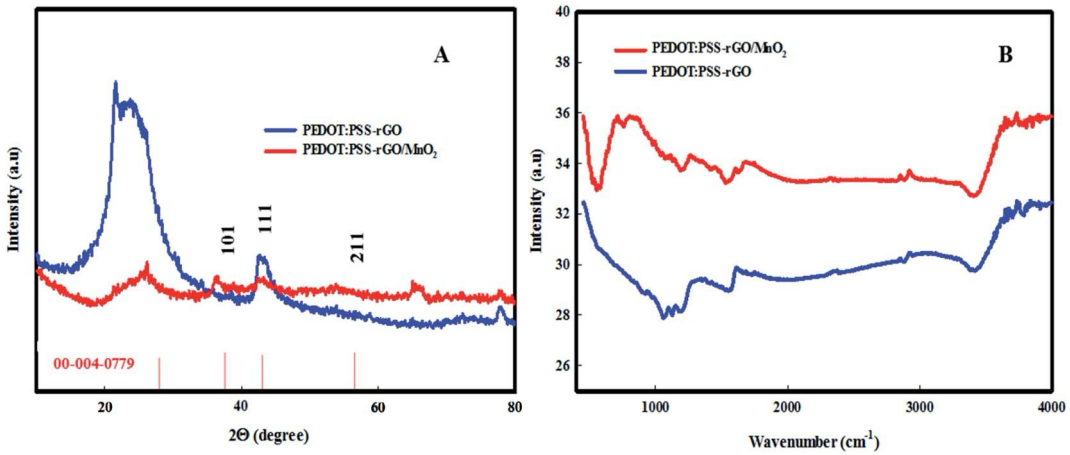


Fig. 4 (A) XRD pattern and (B) FT-IR spectra of the prepared samples.

### 3.2. Electrochemical investigations of the $MnO_2$/PEDOT:PSS–rGO@CF

The electrochemical performances of MnO2, MnO2/PEDOT:PSS, EDOT:PSS–rGO and MnO2/PEDOT:PSS–rGO electrodes were measured by cyclic voltammetry and galvanostatic charge/ discharge tests in 1.0 M $Na_2SO_4$ aqueous electrolyte. Fig. 5A shows cyclic voltammograms (CVs) of the prepared electrodes within the potential range of 0.1 to 0.9 V at a scan rate of15 mV $s^{-1}$. As can be seen in Fig. 5A, the current density and the area under the CV curve are higher for the $MnO_2$/PEDOT:PSS–rGO electrode compared with other prepared electrodes, which indicates the higher capacitive performance of the $MnO_2$/ PEDOT:PSS–rGO electrode due to good interaction among the components of rGO, PEDOT:PSS, and $MnO_2$. CV curves of $MnO_2$/PEDOT:PSS–rGO, $MnO_2$, $MnO_2$/PEDOT:PSS, and PEDOT:PSS–rGO electrodes at various scan rates, ranging from 5 to 35 mV $s^{-1}$, were also recorded and shown, respectively, in Fig. 5B and S1.† The current response for all electrodes increases with increasing the scan rate, which indicates the capacitive behavior of the prepared electrodes. Moreover, CV curves of $MnO_2$/PEDOT:PSS–rGO, PEDOT:PSS–rGO and PEDOT:PSS electrodes display a quasi-rectangular shape with symmetric *I–E* responses, demonstrating good capacitive behavior with the in□uence of pseudo-capacitance characteristics. Also, by increasing the sweep rate, a slight deviation from the rectangular shape can be observed for the $MnO_2$/PEDOT:PSS–rGO electrode due to the restriction of charge propagation within the electrode. The CV curves of $MnO_2$ present a couple of small redox peaks, predicting their faradaic battery-type behavior. The oxidation–reduction reaction for $MnO_2$ is usually described as: $MnO_2 + Na^+ + e^-$ \$ MnOONa. The dependence of the peak current on the scan rate (y) can be used to determine the charge transfer mechanism: $i = ay^b$ (*a* and *b* are adjustable parameters). Observation of a value of 0.5 for *b* represents a total diffusion controlled process, whereas 1.0 indicates a capacitive process or nondiffusion-controlled process. For PEDOT:PSS–rGO and $MnO_2$/PEDOT:PSS–rGO electrodes, the *b*-value was found to be ~0.8 and 0.6, respec
tively, from the slope of the log(y)–log(*i*) plots, which indicates a diffusion-controlled process of the $MnO_2$/PEDOT:PSS–rGO electrode (Fig. 5C). To distinguish quantitatively a fraction of the current arising from capacitive and diffusion contributions, Dunn's method was used based on the following equation:[54–57]

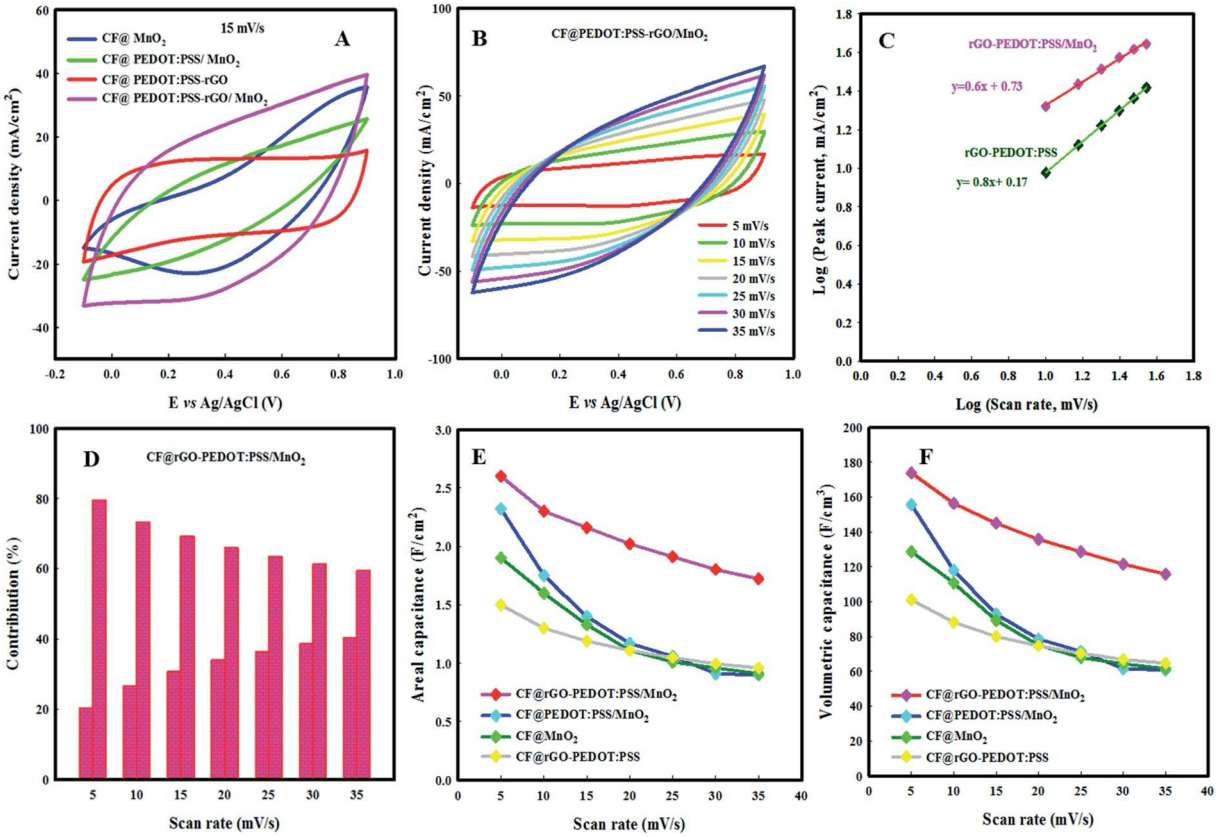


Fig. 5 (A) CV curves of $MnO_2$, $MnO_2$/PEDOT:PSS, PEDOT:PSS–rGO and $MnO_2$/PEDOT:PSS–rGO electrodes at a scan rate of 15 mV $s^{-1}$. (B) Typical CV curves of the $MnO_2$/PEDOT:PSS–rGO electrode at different scan rates. (C) Logarithmic relationship between anodic peak current andscan rate. (D) Comparison of charge storage for the $MnO_2$/PEDOT:PSS–rGO electrode at different scan rates. (E) Areal and (F) volumetric capacitances of $MnO_2$, $MnO_2$/PEDOT:PSS, PEDOT:PSS–rGO and $MnO_2$/PEDOT:PSS–rGO electrodes as a function of scan rate.

$$i \text{ (at fixed V)} = k_1 v + k_2 v^{1/2} \qquad (7)$$

The values of $k_1$ and $k_2$ can be calculated from the slope and intercept of the straight line of $i/y^{1/2}$ *versus* $y^{1/2}$ plot, respectively.

The contribution of diffusion-controlled behavior and the capacitive process of the MnO2/PEDOT:PSS–rGO electrode is 66% and 34%, at a scan rate of 20 mV s 1, respectively, indicating predominant diffusion behavior of the electrode material during the electrochemical processes (Fig. 5D and S2B†).

Formicro-sized fiber-shaped supercapacitors, the geometricalspecific capacitances (length, areal and volumetric) are more reliable and accurate than the mass based gravimetric capacitances. The $C_x$ values obtained from CV curves of the $MnO_2$/ PEDOT:PSS–rGO, $MnO_2$, $MnO_2$/PEDOT:PSS, and PEDOT:PSS–rGO electrodes at a scan rate of 5 mV $s^{-1}$ are 2.6 F $cm^{-2}$ (174 F$cm^{-3}$ and 0.49 F $cm^{-1}$), 1.9 F $cm^{-2}$ (128.6 F $cm^{-3}$ and 0.36F $cm^{-1}$), 2.3 F $cm^{-2}$ (156 F $cm^{-3}$ and 0.43 F $cm^{-1}$), and 1.5 F$cm^{-2}$ (101 $cm^{-3}$ and 0.28 F $cm^{-1}$). At a high scan rate of 35 mV $s^{-1}$, the specific capacitances for these electrodes were, respec-tively, 1.72 F $cm^{-2}$ (116 F $cm^{-3}$ and 0.32 F $cm^{-1}$), 0.91 F $cm^{-2}$ (61 F $cm^{-3}$ and 0.17 F $cm^{-1}$), 0.9 F $cm^{-2}$ (61 F $cm^{-3}$ and 0.17 F $cm^{-1}$), and 0.96 F $cm^{-2}$ (65 F $cm^{-3}$ and 0.18 F $cm^{-1}$) (Fig. 5E,F and S2A†). The results reveal that by increasing the scan rate, the specific capacitances of the electrodes decrease gradually. At lower scan rates, electrolyte ions can diffuse to all active sites ofthe electrode, while at higher scan rates, the inner surface of theactive materials is not

completely used in the electrochemical process and electrolyte ions can only diffuse to the outer surface, which leads to decline in specific capacitance values.[58–61].

To further evaluate the capacitive performance of the prepared electrodes, the GCD measurements were carried out in 1.0 M Na2SO4 aqueous electrolyte within the potential range of 0.1 to 0.9 V at a current density of 5 mA cm-2 (Fig. 6A). The GCD curves of MnO2/PEDOT:PSS–rGO, PEDOT:PSS–rGO and PEDOT:PSS electrodes exhibit a symmetrical triangular shape suggesting good reversibility and ideal capacitive behavior, which are in good agreement with the CV curves. For MnO2, a deviation from the straight line can be observed, in agreement with the CV redox signals mentioned above. A small IR-drop(which can be observed from the voltage drop at the beginning of the discharging process) is observed for the MnO2/PEDOT:PSS–rGO and PEDOT:PSS–rGO electrodes at a current density of 5 mA cm 2, revealing the low resistance of these electrodes. Moreover, the MnO2/PEDOT:PSS–rGO electrode shows a longer discharge time compared with other electrodes such as MnO2, PEDOT:PSS, MnO2/PEDOT:PSS, and PEDOT:PSS–rGO, indicating the higher charge storage capacity of the MnO2/PEDOT:PSS–rGO electrode. The areal, volumetric and length specific capacitance values of the MnO2/PEDOT:PSS–rGO, MnO2/PEDOT:PSS, MnO2, and PEDOT:PSS–rGO electrodes were obtained from GCD measurements and found to be 2.92 F cm-2 (194 F cm-3 and 550 mF cm-1), 2.18 F cm 2 (145 F cm-3 and 410 mF cm-1), 1.64 F cm-2 (109 F cm-3 and 308 mF cm-1), and 0.99 F cm-2 (66 F cm-3 and 187mF cm-1) respectively, at a current density of 5 mA cm-2. The MnO2/PEDOT:PSS–rGO electrode has higher specific capacitance relative to other electrodes, indicating excellent electrochemical performance during charge–discharge processes. The GCD measurements were carried out at different values of current density for MnO2/PEDOT:PSS–rGO, MnO2/PEDOT:PSS, MnO2, and PEDOT:PSS–rGO electrodes, and the results are shown in Fig. 6B, C and S3.† The specific capacitance values of electrodes are estimated as a function of current density, according to eqn (1)–(3) and plotted in Fig. 6D–F.

The specific capacitance values for the $MnO_2$/PEDOT:PSS– rGO electrode at current densities of 5, 6, 12, 16, 20 and 25 mA $cm^{-2}$ are 2.92 F $cm^{-2}$ (194 F $cm^{-3}$ and 550 mF $cm^{-1}$), 2.73 F $cm^{-2}$ (182 F $cm^{-3}$ and 515 mF $cm^{-1}$), 2.3 F $cm^{-2}$ (152 F $cm^{-3}$ and 431 mF $cm^{-1}$), 2.06 F $cm^{-2}$ (136 F $cm^{-3}$ and 386 mF $cm^{-1}$),1.87 F $cm^{-2}$ (124 F $cm^{-3}$ and 352 mF $cm^{-1}$) and 1.7 F $cm^{-2}$ (114F $cm^{-3}$ and 319 mF $cm^{-1}$), respectively. Also, the calculated gravimetric capacitance of the prepared electrode is shown in Fig. S4.† Table S1† shows that the specifific capacitance of the $MnO_2$/PEDOT:PSS–rGO electrode is comparable and evensuperior compared to the previously reported values of $MnO_2$ and PEDOT:PSS composites prepared on different substrates (such as Ni foam, Cu foam and carbon cloth).[38–48,62–70]

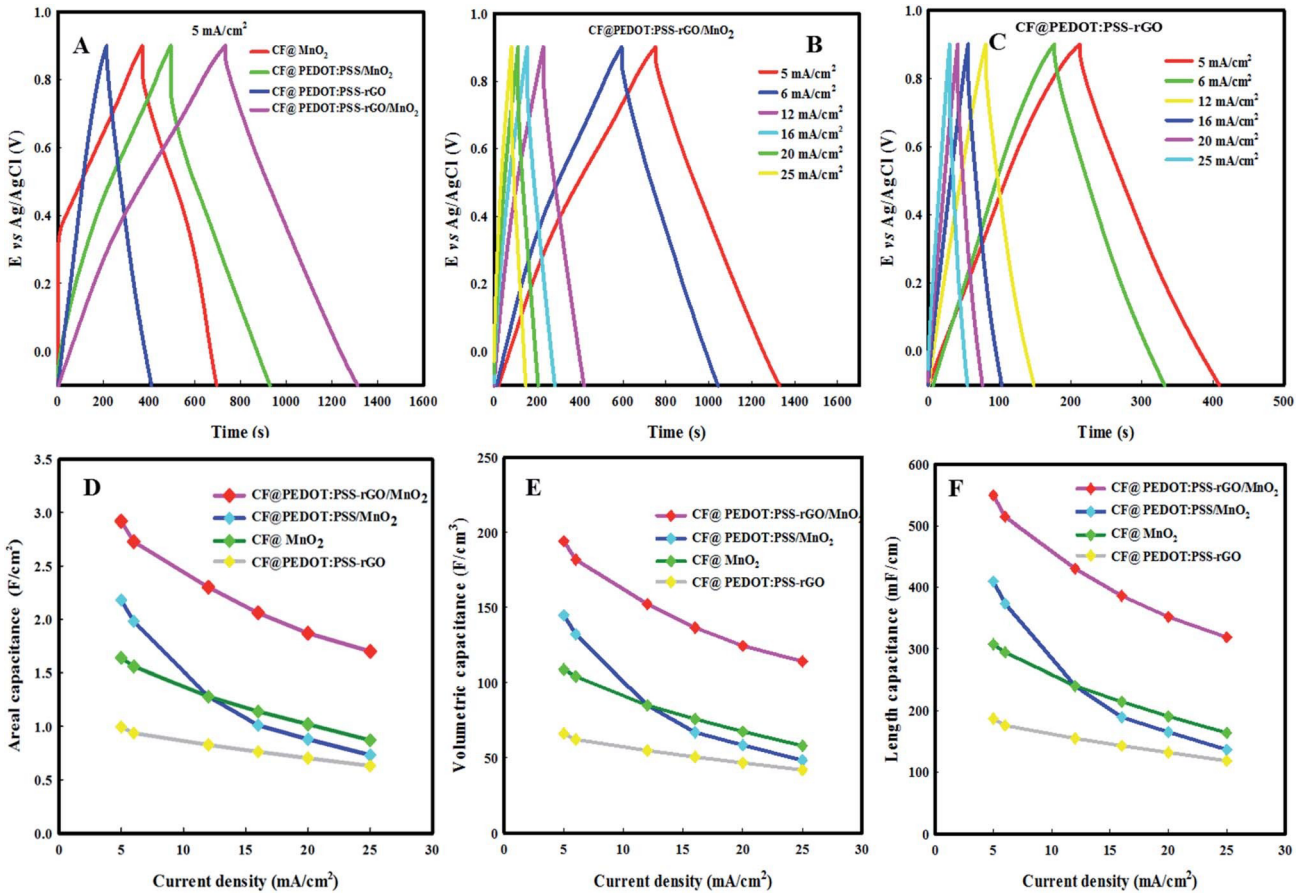


Fig. 6 (A) GCD curves of $MnO_2$, $MnO_2$/PEDOT:PSS, PEDOT:PSS–rGO and $MnO_2$/PEDOT:PSS–rGO electrodes at a current density of 5 mA $cm^{-2}$. (B) Typical GCD curves of the $MnO_2$/PEDOT:PSS–rGO electrode at different current densities. (C) GCD curves of the PEDOT:PSS–rGO electrodeat different current densities. (D) Areal, (E) volumetric, and (F) length capacitances of $MnO_2$, $MnO_2$/PEDOT:PSS, PEDOT:PSS–rGO and $MnO_2$/ PEDOT:PSS–rGO electrodes as a function of current density.

The electrochemical kinetics of the $MnO_2$/PEDOT:PSS–rGO and PEDOT:PSS–rGO electrodes are further studied by the Trasatti analysis method.[71,72] In this procedure, the total voltammetric charge, $q_t$, is composed of the stored charges at the innersurface ($q_i$) or less accessible surface charge and the outer surface charge ($q_o$) or more accessible surface charge ($q_t$ ¼ $q_o$ + $q_i$). The stored charges at the inner surface mainly originate from the less accessible surfaces such as grain, pores, boundaries and cracks and is a diffusion controlled reaction. The outer surface charges mainly originate from the direct accessible surface, which is related to the region directly in contact with the electrolyte solution. The outer surface charge is independent of the scan rate and the reactive species diffusion does not control the reaction.73 The intercept of the linear plot of (1/q) against y1/2 gives the total voltammetry charge, which is obtained at very low scan rates (y/0) and associated with nearly all active sites of the electrode. The stored charges at the outer surface (qo) can be obtained from the intercept of the linear plot of 1/q against y1/2 at very high scan rates (y / N) (Fig. 7A and C). Therefore, stored charges at the inner surface (qi), can be calculated from the difference between qt and qo.74 According to the Trasatti plot (Fig. 7B and D), the total charges of the rGO–PEDOT:PSS/MnO2 and rGO–PEDOT:PSS electrodes are 3.79 C cm 2 and 2.3 C cm-2, respectively, while, the charge stored at the outer surface of these electrodes is found to be 1.3 C cm 2 and 0.66 C cm 2, respectively. Furthermore, the charge stored in the inner active sites of MnO2/PEDOT:PSS–rGO and PEDOT:PSS–rGO electrodes is found to be 2.5 C cm-2 and 1.64 C cm-2, respectively. The high values of charge

stored in the inner surface indicate that most of the surfaces are fully accessible to electrolyte ions with minimum diffusion limitations during the electrochemical processes.62,75

In order to get further insight into the charge transfer kinetics and the ion diffusion in the MnO2/PEDOT:PSS–rGO, PEDOT:PSS–rGO, MnO2/PEDOT:PSS and MnO2 electrodes, EIS analysis was conducted within the frequency range from 100 kHz to 0.01 Hz, and the results are shown in Fig. 7E. The Nyquist plots in Fig. 7E reveal a semicircle in the high frequency region that corresponds to the charge transfer resistance (Rct),which is in turn related to the faradaic processes, and a line in the low frequency region, which is characteristic of the capacitive behavior. In Fig. 7E, the diameter of the semicircle for the MnO2 electrode is the largest among all electrodes, which indicates a low charge transfer rate. Moreover, the line slope of the MnO2/PEDOT:PSS–rGO and PEDOT:PSS–rGO electrodes is much higher than that of MnO2 and MnO2/PEDOT:PSS electrodes, indicating faster diffusion of electrolyte ions from the solution to the electrode surface. Also, the shorter line for the MnO2/PEDOT:PSS–rGO electrode, compared to the other electrodes, is due to its higher capacitive behavior. Therefore, these results demonstrate that the MnO2/PEDOT:PSS–rGO electrode has the best capacitive performance among the other fabricated electrodes.

The long-term cycle stability of MnO2/PEDOT:PSS–rGO and PEDOT:PSS–rGO has been evaluated by repeating the charge–discharge test at a current density of 12 mA cm-2 over 5000 cycles (Fig. 7F and S5A†). The results reveal that MnO2/PEDOT:PSS–rGO and PEDOT:PSS–rGO electrodes retain about 97% and 96% of their initial capacitance values after 5000 charge/discharge cycles, respectively, which demonstrates the excellent stability of the electrodes over cycling. The inset of Fig. 7F shows the GCD curves for the last 30 cycles. The morphology and crystalline structure of the PEDOT:PSS–rGO@CF and MnO2/PEDOT:PSS–rGO@CF electrodes after the cycling process were evaluated by using FE-SEM images and XRD spectra. As shown in Fig. S5B–E,† after successive charge/discharge cycles, the morphology of the electrodes remained unchanged. Moreover, the XRD patterns of the electrodes demonstrated that the composition of electrodes has no change before and after the cycling.

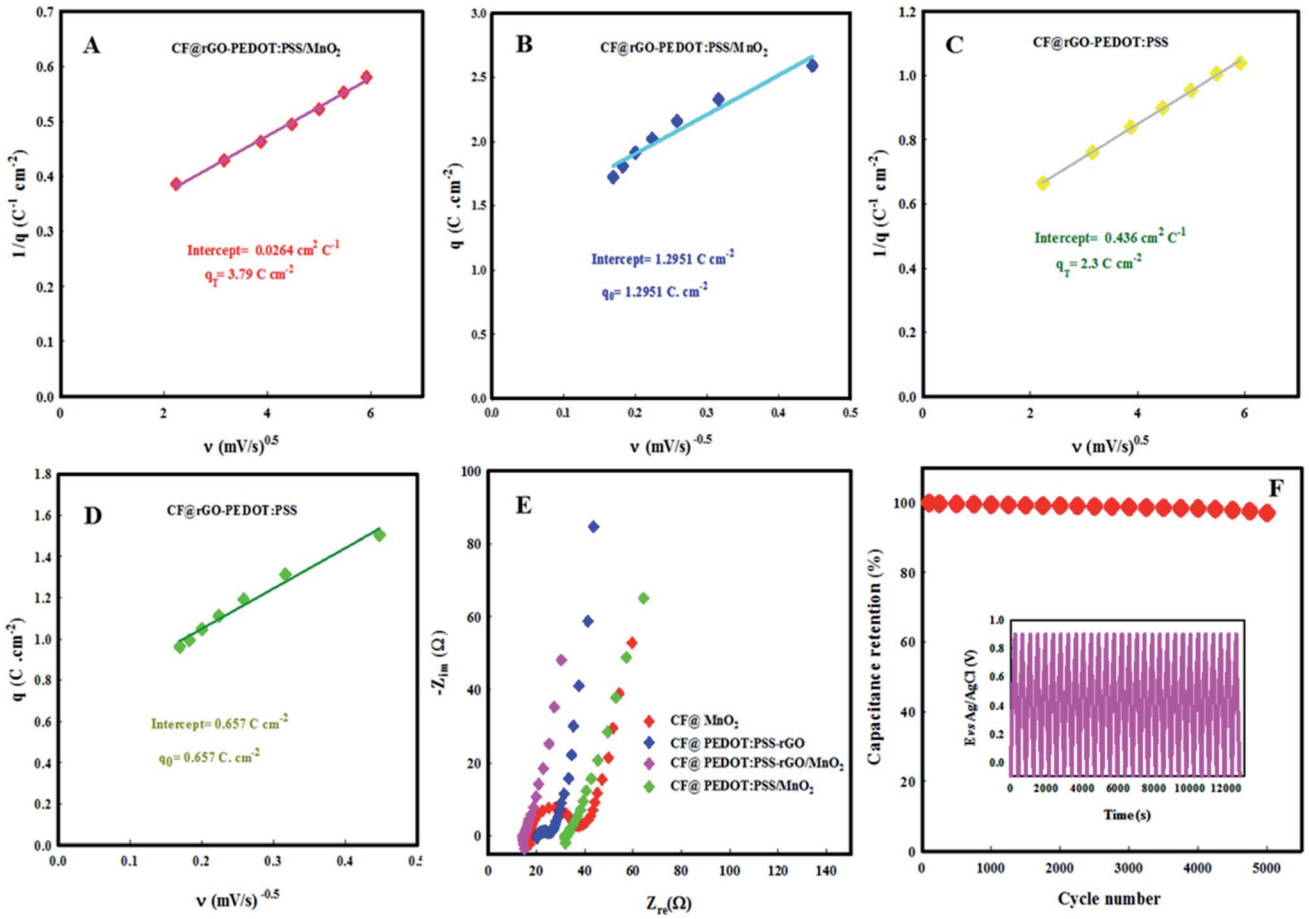


Fig. 7 Trasatti plots of (A) $1/q$(y) against $y^{0.5}$ and (B) $q$(y) against $y^{-0.5}$ of the $MnO_2$/PEDOT:PSS–rGO electrode. Trasatti plots of (C) $1/q$(y) against$y^{0.5}$ and (D) $q$(y) against $y^{-0.5}$ of the PEDOT:PSS–rGO electrode. (E) Nyquist plots of the $MnO_2$, $MnO_2$/PEDOT:PSS, PEDOT:PSS–rGO and $MnO_2$/PEDOT:PSS–rGO electrodes. (F) Long-term cyclic performance $MnO_2$/PEDOT:PSS–rGO electrode at a current density of 12 mA $cm^{-2}$ (inset: corresponding GCD curves of the last 30 cycles).

### 3.3. Electrochemical performance of the fiber-shaped micro-supercapacitor

To evaluate the feasibility of the $MnO_2$/PEDOT:PSS–rGO electrode in supercapacitor applications, a fiber shaped asymmetric micro-device was fabricated using $MnO_2$/PEDOT:PSS–rGO as the positive electrode and PEDOT:PSS–rGO as the negative electrode and $Na_2SO_4$–CMC as the solid-state electrolyte (dis- played as $MnO_2$/PEDOT:PSS–rGO//PEDOT:PSS–rGO). Fig. S6A and D† show the CV and GCD curves of PEDOT:PSS–rGO at various scan rates and current densities, respectively. CV curves of PEDOT:PSS–rGO exhibit relatively rectangular shapes and GCD curves are closely linear and symmetric, indicating an ideal capacitor characteristic and a good reversible behavior.

The calculated areal, volumetric and length capacitance valuesof the PEDOT:PSS–rGO electrode were 1.03 F $cm^{-2}$, 69 F $cm^{-3}$and 193 mF $cm^{-1}$ at a current density of 5 mA $cm^{-2}$, respectively(Fig. S6B, C and E–G†).

To maximize the performance of the fiber-shaped micro- supercapacitor, mass balance between the two electrodes is necessary. The amount of the charge stored by each electrode, $q$, is estimated by using the following equation:

$$Q = C_L \times \Delta V \times L \qquad (8)$$

where DV is the electrode potential working range. Based on this equation, the optimal length for the fiber-shaped micro-device is about $L_+/L_- = 0.4$ in an asymmetric configuration. The CV curves of $MnO_2$/PEDOT:PSS–rGO and PEDOT:PSS–rGO elec- trodes at a scan rate of 15 mV $s^{-1}$ in the three-electrode system showed a stable potential window from —0.8 to 0.4 V for the rGO–PEDOT:PSS electrode and from —0.1 to 0.9 V for the $MnO_2$/PEDOT:PSS–rGO electrode (Fig. 8A). Also, the CV curves of the fiber-shaped micro-devices were investigated in different voltage windows ranging from 0–1.0 V to 0–2.2 V at a scan rate of30 mV $s^{-1}$ (Fig. 8B). As can be seen, the working potential window of the fabricated fiber micro-device can be extended to 2.0 V. Fig. 8C shows the CV curves of the asymmetric micro- device at different scan rates (from 5–35 mV $s^{-1}$) in the potential range of 0–2.0 V in a $Na_2SO_4$–CMC solid-state electrolyte.

The integrated area and current density in CV curves increase with increasing the scan rate. In addition, the rectangular shape of the CV curves was well maintained even at high scan rates, demonstrating an ideal capacitive behavior, the excellent reversibility and the fast charge/discharge properties of the fabricated fiber micro-device. A high specific capacitance of 545 mF $cm^{-2}$ (36 F $cm^{-3}$ and 102 mF $cm^{-1}$) can be achieved ata scan rate of 5 mV $s^{-1}$ and the value remains as high as 401 mF cm-2 (27 F cm-3 and 75 mF cm-1) at a high scan rate of 35 mV s-1 (Fig. 8D).

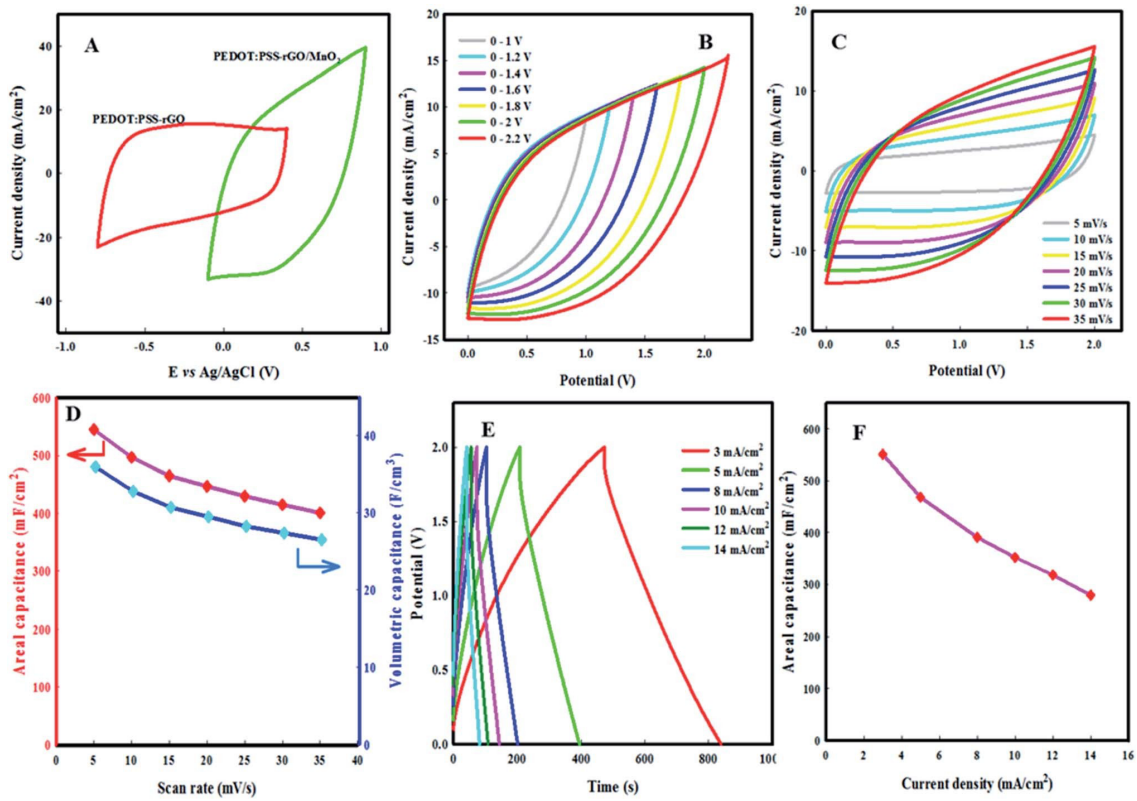


Fig. 8 (A) CV curves of the $MnO_2$/PEDOT:PSS–rGO and PEDOT:PSS–rGO electrodes at 15 mV $s^{-1}$ in a three-electrode system. (B) CV curves ofthe fabricated micro-device in different potential ranges at 30 mV $s^{-1}$ (C) CV curves of the fiber-shaped micro-device at different scan rates. (D)Areal and volumetric capacitance of the micro-supercapacitor as a function of scan rates. (E) GCD curves of the asymmetric micro-device at different current densities. (F) Areal capacitance of the fabricated micro-device as a function of current densities ($Na_2SO_4$–CMC solid-state electrolyte).

The GCD curves of the solid state micro-device at various current densities are shown in Fig. 8E. The triangular shape and symmetry of the GCD curves in a wide potential range also confirm the excellent capacitive behavior of the micro-device. The calculated specific capacitances from GCD curves are displayed in Fig. 8F. Regarding GCD curves at different current densities, the fabricated micro-device shows a remarkable charge–discharge coulombic efficiency and low polarization, indicating high reversibility of the asymmetric fiber micro-supercapacitor.

From the GCD data, areal specific capacitances of 550, 468, 391, 352, 318, and 279 mF cm-2 are obtained for the fabricated fiber micro-device at current densities of 3, 5, 8, 10, 12 and 14 mA cm-2, respectively, equivalent to the volumetric specific capacitance of 35, 30, 26, 23, 21 and 18 F cm-3 at similar current densities (Fig. S7C†). The calculated length specific capacitance values utilizing CV and GCD curves for the fiber-shaped microdevice are plotted in Fig. S7A and B. As can be seen, the specific capacitance decreased gradually with increasing the scan rate and the current density, due to limited ion diffusion, which leads to decreasing utilization of the active materials.

The cycle stability of the asymmetric micro-device was measured by multiple charge/discharge cycles (5000) at 8 mA $cm^{-2}$, and the results are presented in Fig. 9A. The fabricated micro-device retained 96% of its initial capacitance after 5000 cycles, indicating the excellent long-term cycle life of the asymmetric fiber-type supercapacitor.

The energy and power densities, that are the key performance indicators of the fabricated asymmetric micro-device for real applications, were calculated based on their geometry parameters and were plotted on a Ragone diagram (Fig. 9B and S7D†). The fiber shaped micro-device presents an areal energy maximum of 295 microW h cm 2 at 2900 microW $cm^{-2}$ (at a current density of 3 mA $cm^{-2}$) and can maintain an energy density of 150 micro Wh $cm^{-2}$ at a power density of 14 100 micro W $cm^{-2}$ (at a current density of 14 mA $cm^{-2}$). The corresponding volumetric and length energy density of the fabricated micro-device varied from 19 mW h $cm^{-3}$ (55 microW h $cm^{-1}$) to 10 mW h $cm^{-3}$ (29.2 microW h $cm^{-1}$) at power densities of 190 mW $cm^{-3}$ (545 microW $cm^{-1}$) to 930 mW $cm^{-3}$ (2650 microW $cm^{-1}$). The performance values of the fabricated FIbershape micro-device are higher than previously reported values of Ag–PEDOT:PSS/CNT (8.89 microW h $cm^{-2}$),[76] PEDOT-CNT (2.82 microW h $cm^{-2}$),[77] SWCNT/PEDOT:PSS/CuHcF//Mo doped $WO_3$/ SWCNT (30.08 W h $L^{-1}$),[62] PANi/PEDOT/PANi/ultralarge-rGO// PEDOT/$MoS_2$ (5.4 mW h $cm^{-3}$),[47] PEDOT:PSS/$MoS_2$/PEDOT (0.2 microW h $cm^{-2}$ (1.81 mW h $cm^{-3}$)),[63] $MnO_2$@PEDOT:PSS@OCNTF (125.37 microW h $cm^{-2}$),[64] and PEDOT:PSS/rGO (2.24 microW h $cm^{-2}$)[65] (see Table S2† for a detailed comparison).

The flexibility of the asymmetric micro-device was investi- gated by CV measurements under different bending angles (from 0 to 120°) at a scan rate of 30 mV $s^{-1}$. The shapes of all the CV curves in straight and bending states were almost similar to one another, demonstrating the excellent mechanical stability and high flexibility of our fabricated micro-device, which could be utilized in flexible and portable energy storage systems (Fig. 9C). The dependence of the $C/C_0$ (specific capacitances before and after bending) on the bending cycle number for a micro-ASC device is presented in Fig. 9D. The results indicate that the asymmetric micro-device retained 97% of the initial specific capacitance after 500 bending cycles.

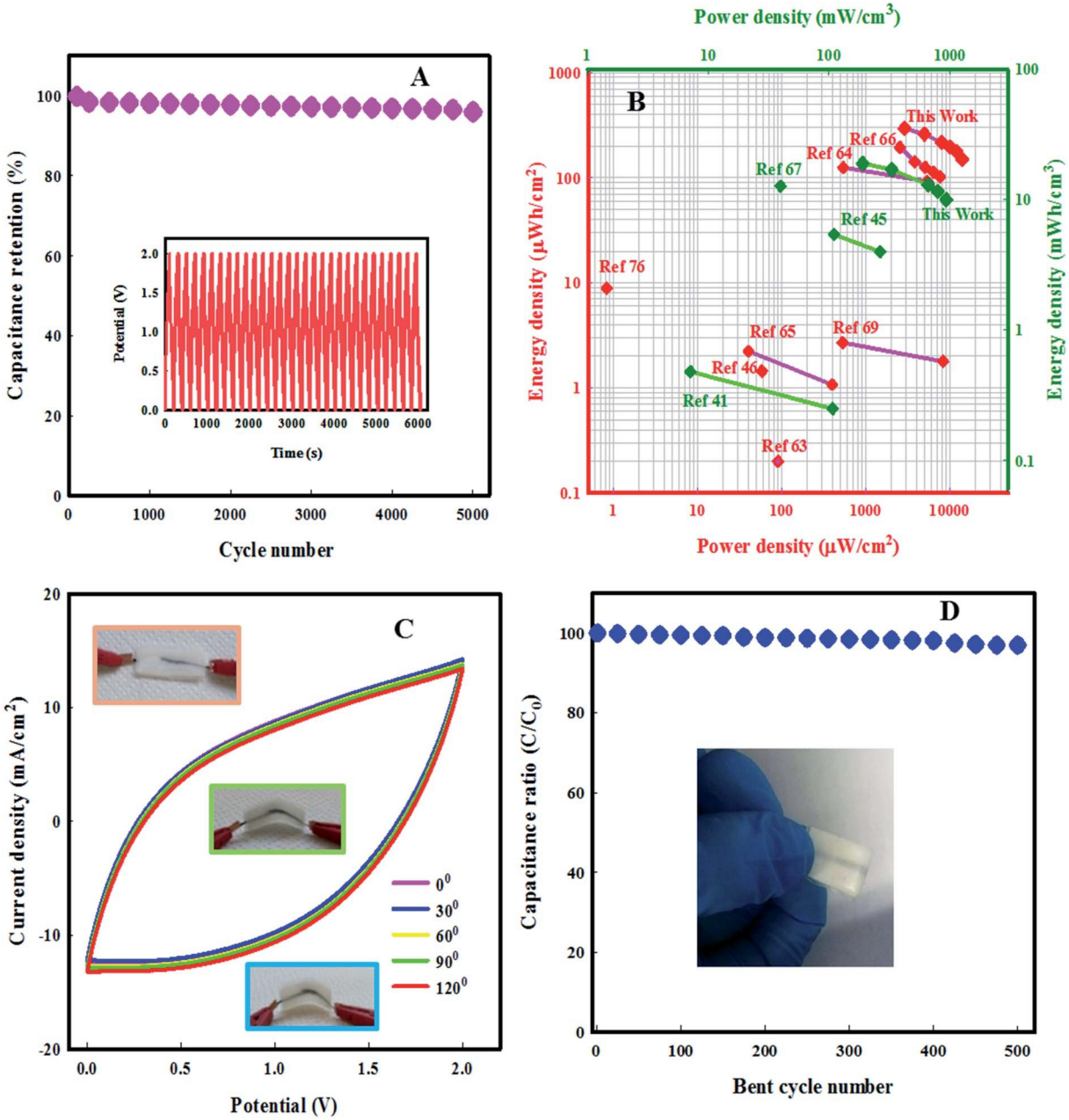


Fig. 9 (A) Cycling performance of the asymmetric micro-device at a current density of 8 mA $cm^{-2}$. (B) Areal Ragone plot of the fiber-shapedmicro-device. (C) CV curves of the solid-state micro-device under straight and different bending states at 30 mV $s^{-1}$. (D) Dependence of specificcapacitance of the solid state micro-device on the bending cycle number. $C_0$ and $C$ correspond to the specific capacitance before and afterbending for different cycles, respectively ($Na_2SO_4$–CMC solid-state electrolyte).

Recently, super-concentrated water-in-salt aqueous electrolytes as a high-voltage approach have attracted many researchers' attention. In high salt concentration, almost all ofthe water molecules are combined with the electrolyte cationsby van der Waals forces, and the amount of free water molecules is reduced, hence the hydrogen and the oxygen evolutions are largely suppressed and make an extended potential window.[78] In this regard, we evaluated electrochemical performance of our micro-device in 27 m KOAC electrolyte. The electrochemical stability windows of $MnO_2$/PEDOT:PSS–rGO@CF and PEDOT:PSS–rGO@CF electrodes are examined by linear sweep voltammetry tests at a scan rate of 10 mV $s^{-1}$ in a three electrode system (Fig. S8†). The $MnO_2$/PEDOT:PSS–rGO@CF electrode in27 m KOAC exhibits a large overpotential for water oxidation

(an extended anodic potential of 1.45 V *vs.* Ag/AgCl) without any indication of the oxygen evolution reaction (OER). The PEDOT:PSS–rGO@CF electrode shows an extended cathodic potential at —1.35 V *vs.* Ag/AgCl, which indicates low electrocatalytic activity towards the hydrogen evolution reaction (HER). Fig. 10A exhibits CV curves at various potential windows from 1.6 to 3.2 V at a scan rate of 30 mV $s^{-1}$ for the fabricated fiber micro-device. The stable electrochemical potential window of the asymmetric micro-device could be extended to 2.8 V in 27 m KOAC electrolyte. The CV curves obtained in 27 m KOAC electrolyte for a potential window of 0–2.8 V at different scan rates are displayed in Fig. 10B. These CV curves show an ideal behavior with rectangular shapes without obvious redox peaks, which are similar to those of the micro-device in $Na_2SO_4$–CMC electrolyte. Fig. 10C shows GCD curves of the asymmetric micro-device at different current densities. The GCD *IR*-drop obtained with 27 m KOAC was higher than that with the $Na_2SO_4$–CMC electrolyte, which indicated a higher internal resistance of the device assembled with the water-in-salt electrolyte. The asymmetric micro-device delivers areal, volumetric and length specific capacitances of 407 mF $cm^{-2}$, 24 F $cm^{-3}$ and 76 mF $cm^{-1}$ at current density of 3 mA $cm^{-2}$, respectively, in 27 m KOAC electrolyte. The flexibility of the flber-shaped micro- device was further examined by mechanical bending tests. As shown in Fig. S9, no performance changes are observed at various bending angles, revealing high flexibility of the micro- SC in 27 m KOAC electrolyte.

The energy and power densities of the fabricated micro- device based on their areal, volumetric and length parameters are shown in Fig. 10D and S10.† At a power density of 3750 microW $cm^{-2}$ (250 mW $cm^{-3}$ and 784 microW $cm^{-1}$), the micro-device with the 27 m KOAC electrolyte delivered a maximum energy of 396 microW h $cm^{-2}$ (26.4 mW h $cm^{-3}$ and 82.8 microW h $cm^{-1}$). At a higher power of 19 740 microW $cm^{-2}$ (3710 microW $cm^{-1}$, 1331.3 mW $cm^{-3}$), the delivered energy was 102 microW h $cm^{-2}$ (6.9 mW h $cm^{-3}$ and 20 microW h $cm^{-1}$). These values were significantly higher than those of the supercapacitors using other highly concentrated elec- trolytes, such as $Ti_3C_2$//a-$MnO_2$ in 21 m KOAC (16.80 mW h $cm^{-3}$ at 137 mW $cm^{-3}$),[31] AC//$MnO_2$ in 21 m Li-TFSI (10 mW h $cm^{-3}$ at 44 mW $cm^{-3}$),[79] AC//AC in 7 m Li-TFSI (6 mW h $cm^{-3}$ at 49 mW $cm^{-3}$),[80] YP-50F//YP-50F in 12 m $NaNO_3$ (20.5 W h $kg^{-1}$),[27] N-rGO fiber in 8.96 M LiCl/PVA (25.6 microW h $cm^{-2}$ (22.7 mW h $cm^{-3}$))[81] and $MnO_2$//$Fe_3O_4$ in 21 m LiTFSI (35.5 W h $kg^{-1}$ at 151.9 W $kg^{-1}$)[82] with an operating voltage of 2.2 V. Also, performance of the asymmetric micro-SC was eval- uated in 12 m $NaNO_3$ electrolyte (Fig. S11†). The constructed asymmetric micro-SC exhibited a maximum energy density of 54 microW h $cm^{-2}$ and power density of 9800 microW $cm^{-2}$ with a working potential of 1.4 V in 12 m $NaNO_3$ electrolyte, which is lower compared to 27 m KOAC (2.8 V) electrolyte. Therefore, an inexpensive and nontoxic potassium-based WSE electrolyte is promising for applications where energy density is critical.

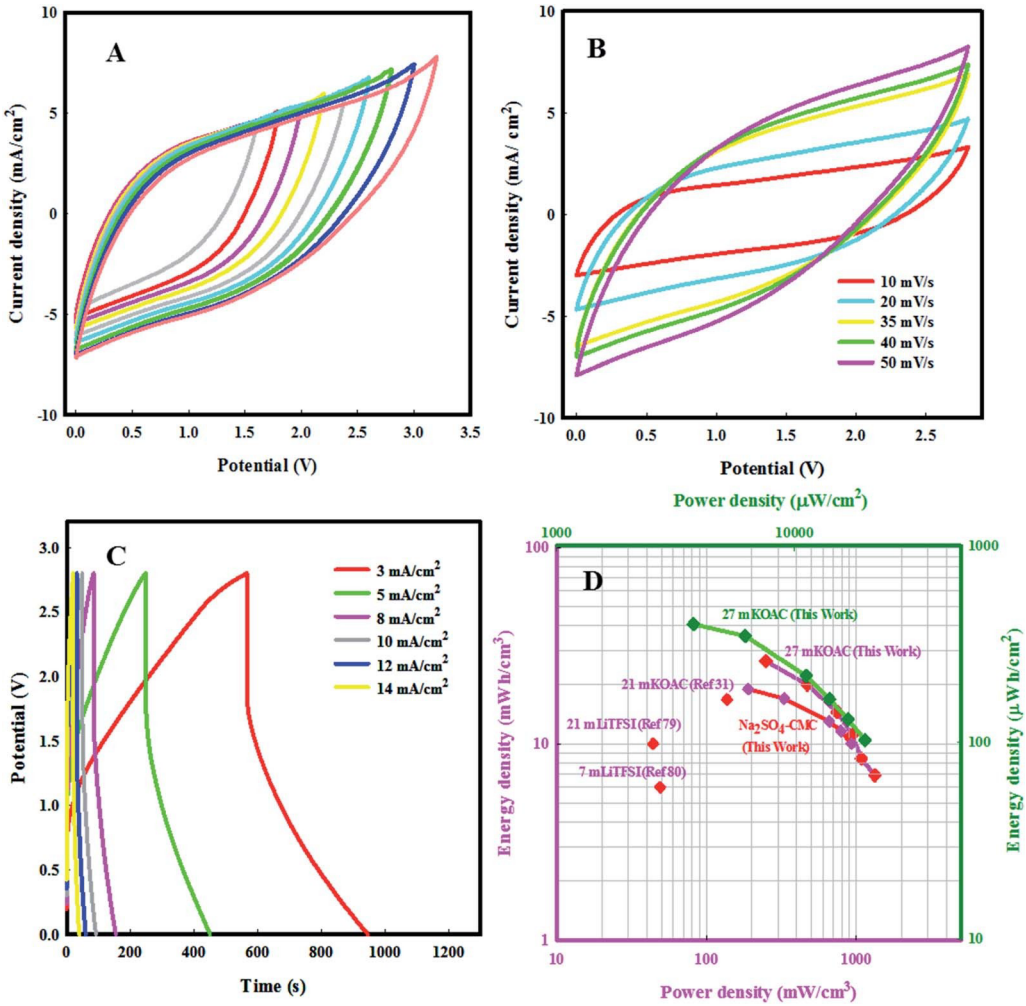


Fig. 10 (A) CV curves of the fabricated micro-device at different potential ranges at 30 mV $s^{-1}$, in 27 m KOAC electrolyte, (B) CV curves of the asymmetric micro-device at various scan rates. (C) GCD curves of the micro-device at different current densities. (D) Areal and volumetric Ragonplot of micro-device (27 m KOAC based-water-in-salt electrolyte).

## 4. Conclusions

A ternary binder-free $MnO_2$/PEDOT:PSS–rGO electrode on a carbon fiber substrate was successfully synthesized by PEDOT:PSS–rGO drop coating and $MnO_2$ electrodeposition. The prepared electrode exhibits a high specific capacitance of 2.92 F $cm^{-2}$ (194 F $cm^{-3}$, 550 mF $cm^{-1}$) at a current density of 5 mA $cm^{-2}$ and excellent cycle stability (95% even after 5000 cycles) in 1 M $Na_2SO_4$ electrolyte. The fiber-shaped asymmetric micro- supercapacitor with $MnO_2$/PEDOT:PSS–rGO and PEDOT:PSS– rGO as positive and negative electrodes presents a stable voltage window of 2 V and delivers an areal, volumetric and length energy density of 295 microW h $cm^{-2}$ (19 mW h $cm^{-3}$ and 55 microW h $cm^{-1}$) at a power density of 2900 microW $cm^{-2}$ (190 mW $cm^{-3}$ and 545 microW $cm^{-1}$) with 96% retention of initial capacity after 5000 cycles in $Na_2SO_4$–CMC solid-state electrolyte. Moreover, a super concentrated potassium acetate-based water-in-salt electrolyte was used to widen the cell voltage window. The micro-device with 27 m KOAC electrolyte can be operated reversibly in a potential window of 0–2.8 V and exhibited an areal, volumetric and length energy density of 396 microW h $cm^{-2}$ (26.4 mW h $cm^{-3}$ and 82.8 microW h $cm^{-1}$) at a power density of 3750 mW $cm^{-2}$ (250

mW $cm^{-3}$ and 784 mW $cm^{-1}$). These results demonstrate the great potential of our constructed micro-device with a water-in-salt electrolyte for practical applications in flexible micro-sized energy storage devices.

## Conflicts of interest

There are no conflicts to declare.

## Acknowledgements

The authors would like to thank the University of Bologna for supporting this work. Also, the authors appreciate the financial support by the Sharif University of Technology, Tehran, Iran.

## References

1 W. Lu, J. Shen, P. Zhang, Y. Zhong, Y. Hu and X. W. D. Lou, *Angew. Chem., Int. Ed.*, 2019, 21, 15441–15447.
2 L. F. Chen, Y. Lu, L. Yu and X. W. D. Lou, *Energy Environ. Sci.*, 2017, 10, 1777.
3 D. Chen, K. Jiang, T. Huang and G. Shen, *Adv. Mater.*, 2019,1901806.
4 Z. Pan, M. Liu, J. Yang, Y. Qiu, W. Li, Y. Xu, X. Zhang andY. Zhang, *Adv. Funct. Mater.*, 2017, 27, 1701122.
5 F. Yi, H. Ren, J. Shan, X. Sun, D. Wei and Z. Liu, *Chem. Soc.Rev.*, 2018, 47, 3152–5188.
6 L. Wang, Q. Wu, Z. Zhang, Y. Zhang, J. Pan, Y. Li, Y. Zhao, L. Zhang, X. Cheng and H. Peng, *J. Mater. Chem. A*, 2016, 4,3217–3222.
7 F. Hekmat, S. Shahrokhian and N. Taghavinia, *J. Phys. Chem. C*, 2018, 122, 27156–27168.
8 H. Hosseini and S. Shahrokhian, *Chem. Eng. J.*, 2018, 341, 10–26.
9 F. Hekmat, H. E. Unalan and S. Shahrokhian, *SustainableEnergy Fuels*, 2020, 4, 643–654.
10 L. Zhang, P. Zhu, F. Zhou, W. Zeng, H. Su, G. Li, J. Gao,R. Sun and C.-P. Wong, *ACS Nano*, 2016, 10(1), 1273–1282.
11 X. Liang, G. Long, C. Fu, M. Pang, Y. Xi, J. Li, W. Han, G. Wei and Y. Ji, *Chem. Eng. J.*, 2018, 345, 186–195.
12 H. Hu, B. Y. Guan and X. W. D. Lou, *Chem*, 2016, 1, 102–113.
13 D. Yu, K. Goh, Q. Zhang, L. Wei, H. Wang, W. Jiang andY. Chen, *Adv. Mater.*, 2014, 26, 6790–6797.
14 N. Jabeen, A. Hussain, Q. Xia, S. Sun, J. Zhu and H. Xia, *Adv. Mater.*, 2017, 29(32), 1700804.
15 P. Yang, Y. Ding, Z. Lin, Z. Chen, Y. Li, P. Qiang, M. Ebrahimi, W. Mai, C. P. Wong and Z. L. Wang, *NanoLett.*, 2014, 14, 731–736.
16 X. Lu, Y. Zeng, M. Yu, T. Zhai, C. Liang, S. Xie, M.-S. Balogun and Y. Tong, *Adv. Mater.*, 2014, 26, 3148–3155.
17 K. Gao, Z. Shao, J. Li, X. Wang, X. Peng, W. Wang andF. Wang, *J. Mater. Chem. A*, 2013, 1, 63–67.
18 J. Yu, W. Lu, J. Smith, K. Booksh, L. Meng, Y. Huang, Q. Li, J. Byun, Y. Oh, Y. Yan and T. Chou, *Adv. Energy Mater.*, 2017, 7, 1600976–1600984.
19 A. Slesinski, K. Fic and E. Frackowiak, *Adv. Inorg. Chem.*,2018, 72, 247–286.
20 T. Y. Kim, H. W. Lee, M. Stoller, D. R. Dreyer,C. W. Bielawski, R. S. Ruoff and K. S. Suh, *ACS Nano*, 2011, 5, 436–442.
21 Z. Zeng, V. Murugesan, K. S. Han, X. Jiang, Y. Cao, L. Xiao, X. Ai, H. Yang, J.-G. Zhang, M. L. Sushko and J. Liu, *Nat.Energy*, 2018, 3, 674–681.
22 Q. Dou, L. Liu, B. Yang, J. Lang and X. Yan, *Nat. Commun.*,2017, 8, 2188.
23 H. Kim, J. Hong, K. Y. Park, H. Kim, S. W. Kim and K. Kang, *Chem. Rev.*, 2014, 114, 11788.
24 M. Bahdanchyk, M. Hashempour and A. Vicenzo, *Electrochim. Acta*, 2020, 332, 135503.
25 J. Y. Luo, W. J. Cui, P. He and Y. Y. Xia, *Nat. Chem.*, 2010, 2,760–765.
26 L. Suo, Y.-S. Hu, H. Li, M. Armand and L. Chen, *Nat. Commun.*, 2013, 4, 1481.
27 J. Guo, Y. Ma, K. Zhao, Y. Wang, B. Yang, J. Cui and X. Yan, *ChemElectroChem*, 2019, 6, 5433–5438.
28 L. Suo, O. Borodin, T. Gao, M. Olguin, J. Ho, X. Fan, C. Luo,C. Wang and K. Xu, *Science*, 2015, 350, 938–943.
29 M. R. Lukatskaya, J. I. Feldblyum, D. G. Mackanic, F. Lissel, D. L. Michels, Y. Cuie and Z. Bao, *Energy Environ. Sci.*, 2018, 11, 2876–2883.
30 D. P. Leonard, Z. Wei, G. Chen, F. Du and X. Ji, *ACS EnergyLett.*, 2018, 3, 373–374.
31 H. Avireddy, B. W. Bylesc, D. Pinto, J. M. D. Galindo, J. J. Biendicho, X. Wang, C. Flox, O. Crosnier, T. Brousse, E. Pomerantseva, J. R. Morante and Y. Gogotsi, *NanoEnergy*, 2019, 64, 103961.

32 D. Yu, Q. Qian, L. Wei, W. Jiang, K. Goh, J. Wei, J. Zhang and Y. Chen, *Chem. Soc. Rev.*, 2015, 44, 647–662.
33 Z. Wang, J. Cheng, Q. Guan, H. Huang, Y. Li, J. Zhou, W. Ni, B. Wang, S. He and H. Peng, *Nano Energy*, 2018, 45, 210.
A. N. Mohamad, L. Carmen, M. Martinez, L. Wang, Z. Sofer, C. Fisher and M. Pumera, *Appl. Mater. Today*, 2017, 9,204–211.
34 R. Wang, Y. Sui, S. Huang, Y. Pu and P. Cao, *Chem. Eng. J.*,2018, 331, 527–535.
35 P. Hu, D. Meng, G. Ren, R. Yan and X. Peng, *Appl. Mater. Today*, 2016, 5, 1–8.
36 D. Pech, M. Brunet, H. Durou, P. Huang, V. Mochalin, Y. Gogotsi, P.-L. Taberna and P. Simon, *Nat. Nanotechnol.*,2010, 5, 651–654.
37 M. Yoonessi, A. Borenstein, M. F. El-Kady, C. L. Turner, H. Wang, A. Z. Stieg and L. Pilon, *ACS Appl. Energy Mater.*,2019, 2, 4629–4639.
38 A. Abas, H. Sheng, Y. Ma, X. Zhang, Y. Wei, Q. Su, W. Lan andE. Xie, *J. Mater. Sci.: Mater. Electron.*, 2019, 30, 10953–10960.
39 A. Liang, D. Li, W. Zhou, Y. Wu, G. Ye, J. Wu, Y. Chang, R. Wang, J. Xu, G. Nie, J. Hou and Y. Dud, *J. Electroanal.Chem.*, 2018, 824, 136–146.
40 Z. Yang, J. Ma, B. Bai, A. Qiu, D. Losic, D. Shi and M. Chen, *Electrochim. Acta*, 2019, 322, 134769.
41 C. Sun, X. Li, J. Zhao, Z. Cai and F. Ge, *Electrochim. Acta*,2019, 317, 42–51.
42 D. Zhao, Q. Zhang, W. Chen, X. Yi, S. Liu, Q. Wang, Y. Liu, J. Li, X. Li and H. Yu, *ACS Appl. Mater. Interfaces*, 2017, 9,13213–13222.
43 Y. Chen, J. Bai, D. Yang, P. Sun and X. Li, *Electrochim. Acta*,2020, 330, 135205.
44 W. H. Khoh, B. H. Wee and J. D. Hong, *Colloids Surf., A*, 2019, 581, 123815.
45 D. Yan, Y. Liu, Y. Li, R. Zhuo, Z. Wu, P. Ren, S. Li, J. Wang, P. Yan and Z. Geng, *Mater. Lett.*, 2014, 127, 53–55.
46 X. Li, C. Zhou, L. Shen, W. Zhou, J. Xu, C. Luo, J. Hou, R. Tanand F. Jiang, *Int. J. Electrochem. Sci.*, 2019, 14, 4632–4642.
47 Y. Chen, J. Xu, Y. Yang, Y. Zhao, W. Yang, X. Mao, X. He andS. Li, *Electrochim. Acta*, 2016, 193, 199–205.
48 J. G. Wang, F. Kang and B. Wei, *Prog. Mater. Sci.*, 2015, 74,51–124.
49 Z. Pan, Y. Qiu, J. Yang, F. Ye, Y. Xu, X. Zhang, M. Liu andY. Zhang, *Nano Energy*, 2016, 26, 610–619.
50 Z. Zhou, Q. Li, L. Yuan, L. Tang, X. Wang, B. He, P. Man, C. Li, L. Xie, W. Lu, L. Wei, Q. Zhang and Y. Yao, *EnergyStorage Materials*, 2020, 25, 893–902.
51 Z. Zhou, Q. Zhang, J. Sun, B. He, J. Guo, Q. Li, C. Li, L. Xieand Y. Yao, *ACS Nano*, 2018, 12, 9333–9341.
52 B. E. Conway, *Electrochemical Supercapacitors and Their Complementarity to Fuel Cells and Batteries*, Wiley, New York, 2010.
53 Y. Wang, Y. Song and Y. Xia, *Chem. Soc. Rev.*, 2016, 45, 5925–5950.
54 L. Kong, C. Zhang, J. Wang, W. Qiao, L. Ling and D. Long, *ACS Nano*, 2015, 9, 11200–11208.
55 S. Shahrokhian and L. Naderi, *J. Phys. Chem. C*, 2019, 123,21353–21366.
56 H. Hosseini and S. Shahrokhian, *Appl. Mater. Today*, 2018, 10, 72–85.
57 Y. W. Li, J. H. Yao, E. Uchaker, M. Zhang, J. J. Tian, X. Y. Liu and G. Z. Cao, *J. Phys. Chem. C*, 2013, 117, 23507–23514.
58 J. Chen, L. Yanga, S. Fang, S. I. Hirano and K. Tachibana, *J. Power Sources*, 2012, 200, 59–66.
59 Y. W. Li, J. H. Yao, C. J. Liu, W. M. Zhao, W. X. Deng and S. K. Zhong, *Int. J. Hydrogen Energy*, 2010, 35, 2539–2545. 61 S. Shahrokhian, R. Mohammadi and M. K. Amini, *Electrochim. Acta*, 2016, 206, 317–327.
62 J. Li, H. Li, J. Li, G. Wu, Y. Shao, Y. Li, Q. Zhanga and H. Wang, *J. Power Sources*, 2018, 386, 96–105.
63 Y. Chen, X. Zhu, D. Yang, P. Wangyang, B. Zeng and H. Sun, *Electrochim. Acta*, 2019, 298, 297–304.
64 Q. Zhanga, J. Sun, Z. Pan, J. Zhang, J. Zhao, X. Wang, C. Zhang, Y. Yao, W. Lu, Q. Li, Y. Zhang and Z. Zhang, *Nano Energy*, 2017, 39, 219–228.
65 W. Yan, J. Li, G. Zhang, L. Wang and D. Ho, *J. Mater. Chem. A*, 2020, 8, 554–564.
66 S. Shahrokhian, L. Naderi and R. Moammadi, *ACSSustainable Chem. Eng.*, 2018, 6, 14574–14588.
67 W. Gong, B. Fugetsu, Z. Wang, T. Ueki, I. Sakata, H. Ogata, F. Han, M. Li, L. Su, X. Zhang, M. Terrones and M. Endo, *Carbon*, 2019, 154, 169–177.
68 S. Jianga, S. Cheng, Y. Huang, T. Shi and Z. Tang, *Ceram. Int.*, 2017, 43, 7916–7921.
69 J. Noh, C. M. Yoon, Y. K. Kim and J. Jang, *Carbon*, 2017, 116,470–478.
70 A. Rafique, A. Massa, M. Fontana, S. Bianco, A. Chiodoni, C. F. Pirri, S. Hernández and A. Lamberti, *ACS Appl. Mater. Interfaces*, 2017, 9, 28386–28393.
71 S. Ardizzone, G. Fregonara and S. Trasatti, *Electrochim. Acta*,1990, 35, 263–267.

72 X. Deng, J. Li, Z. Shan, J. Sha, L. Ma and N. Zhao, *J. Mater. Chem. A*, 2020, 8, 11617–11625.
73 A. K. Singh, D. Sarkar, K. Karmakar, K. Mandal and G. G. Khan, *ACS Appl. Mater. Interfaces*, 2016, 8, 20786–20792.
74 M. Sathiya, A. S. Prakash, K. Ramesha, J. M. Tarascon andA. K. Shukla, *J. Am. Chem. Soc.*, 2011, 133, 16291–16299.
75 L. Naderi and S. Shahrokhian, *J. Colloid Interface Sci.*, 2019, 542, 325–338.
76 Y. Zhu, N. Li, T. Lv, Y. Yao, H. Peng, J. Shi, S. Cao and T. Chen, *J. Mater. Chem. A*, 2018, 6, 941.
77 M. Tahir, L. He, W. Ali Haider, W. Yang, X. Hong, Y. Guo, X. Pan, H. Tang, Y. Li and L. Mai, *Nanoscale*, 2019, 11, 7761–7770.
78 T. Brousse, M. Toupin, R. Dugas, L. Athouel, O. Crosnier and D. Belanger, *J. Electrochem. Soc.*, 2006, 153, A2171–A2180. 79 A. Gambou-Bosca and D. Bélanger, *J. Power Sources*, 2016, 326, 595–603.
80 P. Lannelongue, R. Bouchal, E. Mourad, C. Bodin, M. Olarte, S. le Vot, F. Favier and O. Fontaine, *J. Electrochem. Soc.*, 2018, 165, A657–A663.
81 Q. Liu, J. Zhou, C. Song, X. Li, Z. Wang, J. Yang, J. Cheng, H. Li and B. Wang, *Energy Storage Materials*, 2020, 24, 495–503.
82 M. Zhang, Y. Li and Z. Shen, *J. Power Sources*, 2019, 414, 479–485.